TRACE ELEMENT CONTROL IN BINARY Ni-25Cr AND TERNARY Ni-30Co-30Cr MASTER ALLOY CASTINGS

Martin Detrois[1,2] and Paul D. Jablonski[1,3]

[1] National Energy Technology Laboratory; 1450 Queen Ave. SW; Albany, OR 97321, USA
[2] ORISE – [3] U.S. Department of Energy

Keywords: Master alloy, Electro-slag remelting (ESR), Melt addition, Sulfur, Oxygen, Nitrogen

Abstract

Electro-slag remelting (ESR) is used for control of unwanted elements in commercial alloys. This study focuses on master alloys of Ni-25Cr and Ni-30Co-30Cr, processed through a combination of vacuum induction melting (VIM) and electro-slag remelting (ESR). Minor additions were made to control tramp element levels and modify the melting characteristics. Nitrogen and sulfur levels below 10 ppm and oxygen levels below 100 ppm were obtained in the final products. The role of the alloy additions in lowering the tramp element content, the resulting residual inclusions and the melting characteristics were determined computationally and confirmed experimentally. Additions of titanium were beneficial to the control of oxygen levels during VIM and nitrogen levels during ESR. Aluminum additions helped to control oxygen levels during remelting, however, aluminum pickup occurred when excess titanium was present during ESR. The usefulness of these master alloys for use as experimental remelt stock will also be discussed.

Introduction

The fabrication of clean alloys has been a continuous challenge in casting metallurgy and has been pressured by the increasing performance requirements of novel material designs. In the aerospace industry, the projected increase in the operating temperature of next-generation turbine engines to reduce emissions and improve efficiencies is associated with a need for greater thermo-mechanical properties of Ni-based superalloy components [1]. In the design of high-entropy alloys, several principal elements, or elements at high concentrations [2], can lead to an increase in the tramp element content during casting. Therefore, the amount of tramp and trace elements within the composition of a material needs to be carefully controlled to ensure optimal thermo-mechanical properties of components in service.

Oxygen must be controlled at the ppm level to prevent the formation of residual oxides during casting. When present in the microstructure of the alloy, such inclusions have been reported to act as fatigue crack nucleation sites in Ni-based superalloys and impaired the mechanical properties [3]. Sulfur affects the performance of Ni-based superalloys in various ways and must be carefully controlled [4]. Particularly, sulfur enrichment of the alloy can be detrimental to oxide scale adhesion [5], can decrease grain boundary ductility [6], can embrittle the γ/γ′ interface [7] or form unwanted phases [8]. Nitrogen levels have been of greater concern in Ni-based superalloy castings due to the low solubility of nitrogen in Ni and therefore, in the γ matrix [9]. Thus, alloys that contain nitride formers such as Ti, Nb or Ta are prone to the formation of nitrogen-rich inclusions of sizes in the range of affecting the material's mechanical properties. With relatively large sizes, nitrides such as TiN can adversely affect the properties of various alloys [10].

Several ways of reducing the concentration of tramp elements exist. Among them, selection of the melt stock is of upmost importance. The use of ultra-high purity remelt materials leads to lower oxygen content, particularly in alloys with high Cr concentrations. However, this results in a substantial increase in cost of the final product and is mostly avoided in the industry. For this reason, only industrial-purity melt stock is considered in this investigation. Highly reactive elements such as La and Y can be added to the melt, however, this can also lead to the formation of unwanted phases [3]. Because raw metals such as Cr typically contain a relatively high amount of tramp elements in addition to having a high melting temperature, one approach is to melt binary or ternary master alloys that will be subsequently used in the final alloy design. For instance, the affinity of Cr for oxygen is a concern during the primary melting of high-Cr content alloys. Thus, Cr is often combined with Ni prior to the melting of the final alloy, not only because of the considerable difference in melting temperature between Ni and Cr but also to facilitate the removal of excess tramp elements. Finally, remelting processes such as ESR are commonly used in metal refinery and are particularly efficient at removing tramp elements and impurities [11,12]. During ESR, drops of liquid metal are superheated as they travel through the slag from the ESR electrode to the forming ingot. The various reactions occurring, coupled with the floatation of inclusions, provide an effective way of reducing the amount of impurities in the final ingot.

In this investigation, two master alloys, Ni-25Cr and Ni-30Co-30Cr, were processed using a combination of VIM and ESR. In addition to the base, small amounts of certain elements were added to the master alloys for trace element control and to modify the solidification characteristics. The computational work that led to the selection of the trace element additions will first be described. Then, the experimental results from the two master alloys will be presented for each melt processing step. The role of the trace element additions will be confirmed and discussed by comparison of the computational and experimental work. Finally, the practical use of the master alloys as remelt stock will be presented.

Computational Work and Theory

Carbon additions

The thermodynamic prediction software Thermo-Calc was used with the TCNI8 database version 8 for various simulations of phase diagrams and solubility limit plots [13,14]. Figure 1 represents temperature versus mass percent carbon added to the binary Ni-25Cr master alloy. In the simple binary of Ni-25Cr alloy, the melt range is significantly narrow and only spans 4°C. To improve the

solidification characteristics, C can be added to the composition of the master alloy. In Figure 1, the melt range is greatly expanded by a factor 6 to 24°C when 300 ppm C is added to the binary alloy composition.

Aluminum additions

Most common metallurgical fluxes (i.e., slags) consist of CaF_2, CaO, and Al_2O_3. The slag used for these experiments consists of CaF_2 30% CaO 30% Al_2O_3, Table I. As the slag reacts with the liquid metal drops traveling from the electrode to the forming ingot, the reactions occurring at the metal/slag interface can be improved by optimizing the slag chemistry. One of the major benefits of ESR is known to be the desulfurization capabilities of the slag which can be expressed by the slag/metal reaction of Equation 1:

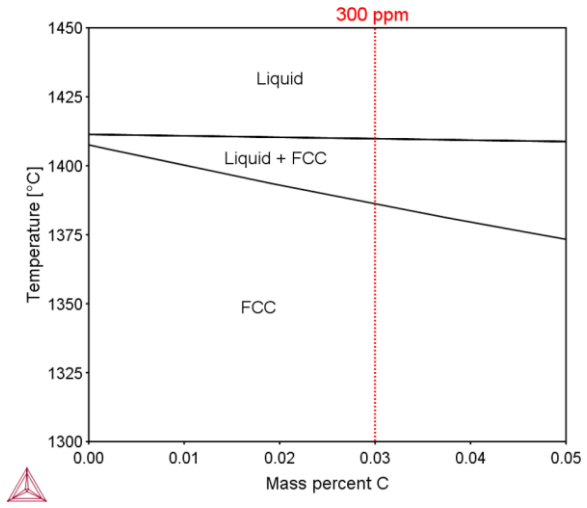

Figure 1. Phase diagram for C additions in the binary Ni-25Cr alloy.

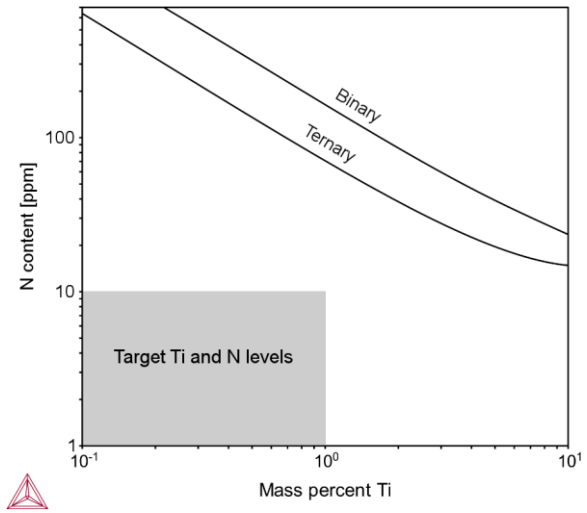

Figure 2. TiN solubility limit at 1450°C for segregation upon solidification in the binary and ternary alloys with the targeted range of Ti and N levels.

$$[S]_{metal} + (CaO)_{slag} \rightarrow (CaS)_{slag} + [O]_{metal} \quad (1)$$

Sulfur is transferred to the slag via an exchange of oxygen to the liquid metal [15]. To improve this reaction, the slag can be deoxidized prior to the ESR process by degassing through heat treatment under vacuum. Additionally, Al granules can be added to the slag in the feeder to deoxidize both the slag and the metal.

Titanium additions

Chrome has a high affinity for oxygen and industrial grade Cr may contain levels of 500-1000 ppm or more. The Cr used to make the master alloys in this work contained over 5200 ppm O. Thus, removing oxygen from the master alloy during the first VIM step is critical. A low oxygen electrode is essential to prevent transportation of oxygen to the slag-ingot interface during remelting where formation of inclusions could occur [16] and compete with sulfur removal [15]. Ti is a known deoxidizer and its effect can be illustrated using the reaction of Equation 2:

$$[Ti]_{metal} + (O_2)_g \rightarrow [TiO_2]_{metal} \quad (2)$$

During VIM, Ti can react with the contained oxygen to form titanium oxides since the Gibbs energy of the oxidation reaction of Ti is thermodynamically favored at –634 kJmol^{-1} compared to that of Cr at –455 kJmol^{-1}, when taken at the pour temperature. Besides oxygen, Cr also has a strong affinity for nitrogen. Commercial purity Cr typically contains from 20 to 500 ppm nitrogen and the Cr used in these experiments contained 50 ppm nitrogen. Adding Ti to the master alloy is expected to be beneficial to oxygen removal, however, Ti often reacts with nitrogen to form TiN. Solubility limit plots for TiN were obtained at the targeted pour temperature for the binary and ternary master alloys and are represented in Figure 2. From the predictions, the expected nitrogen levels and Ti additions should remain below the solubility lines to avoid forming TiN in the liquid metal. From the CALPHAD predictions, additions of Ti at or below 1 wt.% can be made while avoiding formation of TiN during superheat if the nitrogen levels are at or even slightly higher than target levels. Finally, although Ti-nitrides will most likely form during cooling [17], the inclusions after solidification of the VIM ingots can be removed during subsequent ESR.

Inclusion motion

The computational fluid dynamics (CFD) software MeltFlow-ESR from Innovative Research, LLC [18] was used to simulate and represent the remelting of master alloy electrodes. The simulations were ran using the dimensions of ingots, electrodes and crucibles used during ESR at NETL. Carbon and nitrogen were considered in the composition of the alloys at 300 ppm and 10 ppm, respectively. Subsequently, several simulations were run to study the effect of Ti additions in the binary alloy at 0, 0.5, and 1.0 wt.% and in the ternary alloy at 1.0 wt.%. The thermodynamic and thermo-physical properties necessary to the simulations were calculated using Thermo-Calc and JMatPro [19] for each alloy composition, along with the slag properties [18]. Those consisted of the electrode density at room temperature, liquid and solid

Table I. Slag chemistry (wt.%).

CaF_2	CaO	MgO	Al_2O_3	SiO_2	C	S	MnO_2	Fe	TiO_2	P	LOI
38.94	31.50	0.691	28.81	0.16	0.001	0.013	0.006	0.054	0.102	<0.01	0.036

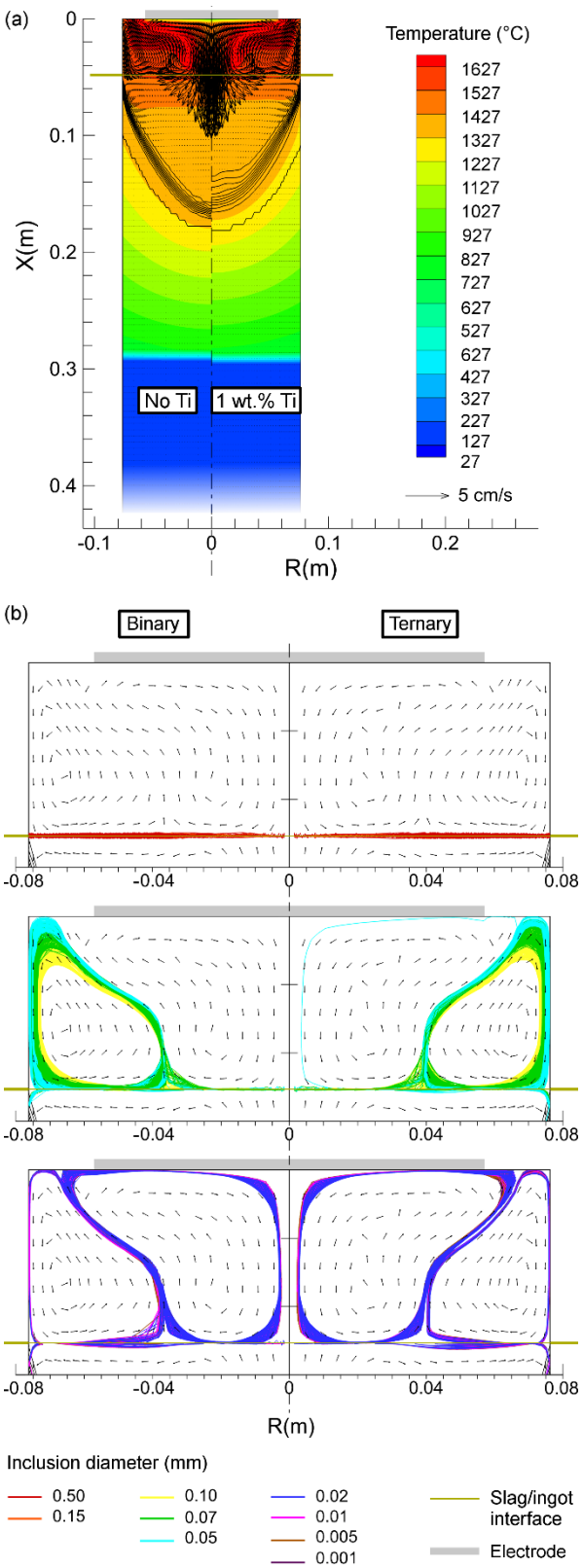

Figure 3. MeltFlow analysis with (a) temperature gradient along the ingot and slag region with velocity vectors for the binary alloy with no Ti and 1 wt.% Ti addition and (b) inclusions trajectories in the binary and ternary alloys.

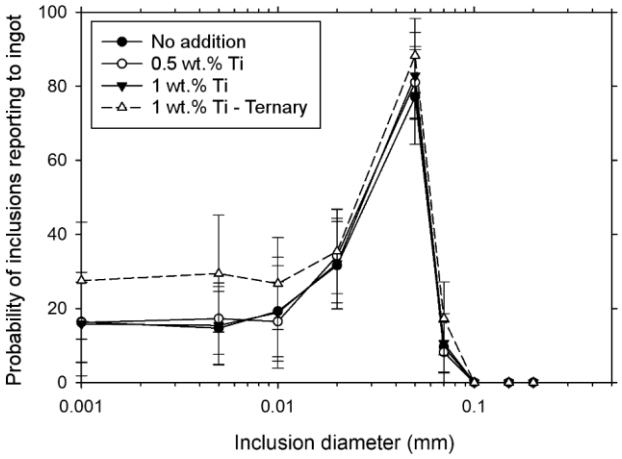

Figure 4. Percent inclusions reporting to the ingot during ESR for a given particle diameter measured in the simulations. Results are averages over the steady state regime and 5 relative densities with error bars representing the standard deviations.

densities, volume expansion coefficient, solidus and liquidus temperatures, latent heat, partitioning coefficients, electrical conductivity, thermal conductivity vs T, specific heat vs T, viscosity vs T and solid fraction vs T, where T is the temperature ranging from room temperature to T_L + 50°C, where T_L is the liquidus temperature. The melting conditions used in the simulations were extracted from the recorded data during ESR experiments and consisted of the melt rate measured, the current set point and the voltage set point over 12 4 min-long time intervals. Lastly, inclusions were considered in the simulations using a range of inclusion densities close to the density of TiN, ρ_{TiN}. The calculations were performed for relative particle densities equal to $0.8\rho_{TiN}/\rho$, $0.9\rho_{TiN}/\rho$, $1.0\rho_{TiN}/\rho$, $1.1\rho_{TiN}/\rho$, and $1.2\rho_{TiN}/\rho$, where ρ is the liquid density of the electrode. Additionally, the percent of inclusions reporting to the ingot was calculated for each ESR process and each particle diameter. The results are an average over 21 iterations in the steady state from 10 to 30 min for all 5 densities.

Temperature contour plots during steady state of remelting are presented in Figure 3a for the binary alloy with no Ti addition and 1 wt.% Ti and represent the slag cap and the forming ingot. The contours are similar with minor differences in the temperature range 1527 to 1227°C. This can be better observed using the liquid fraction lines from 0 to 100% liquid which also reveal the melt pool. Although the shape and depth of the pools are similar for both alloys, the liquid fraction lines are more spread out in the alloy with 1 wt.% Ti resulting in a larger mushy zone. Similar to the effect of C in Figure 1, Ti additions allowed for a wider melt range. The velocity fields were found to be similar for both alloys and revealed significantly higher velocities in the slag, below the electrode, close to the slag/ingot interface. Magnified plots of the slag region are represented in Figure 3b with a comparison between the binary and ternary alloys with 1 wt.% Ti. The velocity field revealed the two loops found in the slag during ESR [20]. The inclusion trajectories were plotted for the various inclusion diameters and separated by size for clarity. Larger inclusions of diameter greater than 100 µm were found to remain at the slag/ingot interface and do not propagate into the ingot, Figures 3b and 4. Medium sized particles were predicted to travel around the outer loop with a maximum probability to penetrate into the ingot for the inclusions of diameter

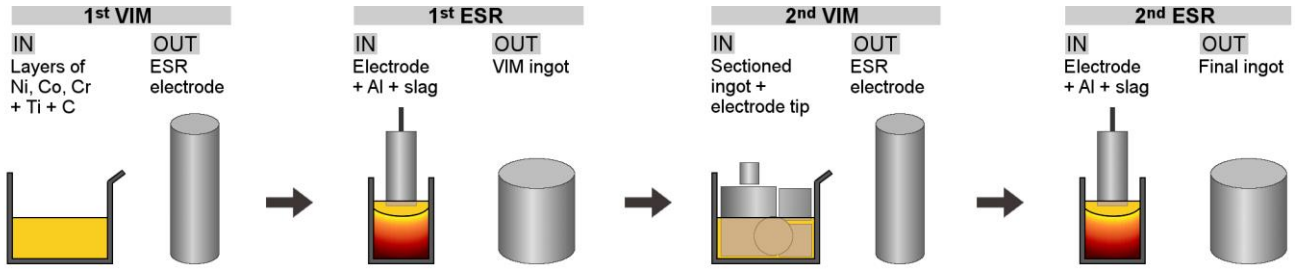

Figure 5. Schematic diagram representing the different steps of the melting process.

~50 µm. Finally, the smaller inclusions of diameter below 50 µm would mainly travel around the inner loop, below the electrode with a relatively low probability of going into the ingot. Although the Ti content is not predicted to influence the inclusion motion in the binary alloy, Figure 4, the simulation gives an insight on the critical size inclusions (~50 µm diameter) during VIM. Additionally, a higher probability of smaller size inclusions going into the ingot was predicted for the ternary alloy, Figure 4, which suggests that lower Ti additions should be considered for the ternary alloy than in the binary alloy to further avoid forming TiN during VIM. Finally, the error bars from Figure 4 originated from averaging over the 21 melt times in the steady state and the 5 relative densities. This allowed for a larger dataset. Although little variations were observed with respect to the melt time, a trend was observed concerning the density of the inclusions. The critical inclusion diameter was found to move towards smaller sizes with increasing particle density.

Experimental Procedure

The two master alloys, Ni-25Cr and Ni-30Co-30Cr, were manufactured using commercial-purity raw starting materials weighted to match the target composition and of total weight of approximately 75 kg. The melt process consisted of two iterations of VIM and ESR and is represented in the schematic diagram of Figure 5. For both alloys, layers of raw Ni and Cr – and Co for the ternary alloy – were placed in the alumina crucible along with C around the center and Ti at the top. Approximately 300 ppm of C and 1.0 wt.% of Ti were added to the binary composition and 300 ppm of C and 0.5 wt.% of Ti were added to the ternary composition. Each alloy was vacuum induction melted and held to the prescribed time and temperature with a superheat temperature of T_L + 50°C. Each melt was poured into 114 mm diameter steel molds to form ESR electrodes. Each electrode was subsequently remelted into a 152 mm diameter crucible under cover gas of argon. The remelting process was initiated using a compact made from turnings of the alloy and layers of slag placed on top of a base disc cut from the VIM ingot [21]. The slag used in this investigation consisted of CaF_2 30% CaO 30% Al_2O_3, previously degassed in a steel retort under vacuum at 450°C and 520°C for 1h each and finally 800°C for 0.5h with a ramp rate of 1°C/min. Additionally, approximately 0.07 wt.% Al granules (45g) were added to the feeder along with additional slag. The feeder was emptied from the initiation of the arc up until the beginning of steady state. Each resulting 152 mm diameter ingot was sectioned and both the VIM and the ESR processes were repeated with no additions during VIM and the Al addition during ESR.

Chemical analysis was performed after each melt on 2 mm thick slices sectioned from the VIM ingot bottom, and approximately 40 mm from the top of the as-cast ESR ingot. The metal chemistries were obtained by x-ray fluorescence (XRF) using a Rigaku ZSX Primus II, with NIST traceable standards (reported values are accurate to 0.01 wt.%). Carbon and sulfur chemistries were determined with a LECO CS444LS using NIST certified standards (reported values are accurate to 10 ppm for C and 1 ppm for S). Oxygen and nitrogen chemistries were determined with a LECO TC436AR using NIST certified standards (reported values are accurate to 1 ppm). Finally, microstructural analysis was performed

Table II. Chemistry results showing the amount of Ni, Cr, Co, Ti, Al and C at each step for the melting process.

Melt		Ni (wt.%)	Cr (wt.%)	Co (wt.%)	Ti (wt.%)	Al (wt.%)	C (ppm)
Ni-25Cr							
1st VIM	IN	Bal.	24.7	-	1.00	-	323
	OUT	Bal.	24.4	<0.001	0.76	0.01	350 ± 7
1st ESR	IN	-	-	-	-	0.07	-
	OUT	Bal.	24.4	<0.001	0.52	0.07	357 ± 10
2nd VIM	IN	-	-	-	-	-	-
	OUT	Bal.	24.4	<0.001	0.53	0.13	349 ± 30
2nd ESR	IN	-	-	-	-	0.08	-
	OUT	Bal.	24.5	<0.001	0.44	0.12	377 ± 48
Ni-30Co-30Cr							
1st VIM	IN	Bal.	29.8	29.8	0.50	-	262
	OUT	Bal.	29.7	30.4	0.24	0.02	289 ± 4
1st ESR	IN	-	-	-	-	0.07	-
	OUT	Bal.	29.7	30.4	0.12	0.04	322 ± 75
2nd VIM	IN	-	-	-	-	-	-
	OUT	Bal.	29.4	30.1	0.17	0.05	303 ± 30
2nd ESR	IN	-	-	-	-	0.07	-
	OUT	Bal.	29.4	30.2	0.10	0.05	290 ± 2

*IN for each step represents the input = prior output (OUT) + additions in the relative line of the Table.

Table III. Chemistry results showing the amount of N, O, and S at each step for the melting process with standard deviations.

Melt		N (ppm)	O (ppm)	S (ppm)
Ni-25Cr				
1st VIM	IN	13	1318	42
	OUT	8 ± 3	103 ± 86	44 ± 3
1st ESR	OUT	10 ± 3	66 ± 56	19 ± 1
2nd VIM	OUT	5 ± 4	46 ± 22	15 ± 1
2nd ESR	OUT	5	31	6 ± 2
Ni-30Co-30Cr				
1st VIM	IN	16	1596	63
	OUT	2 ± 1	76 ± 32	50 ± 2
1st ESR	OUT	4 ± 2	67 ± 26	20 ± 4
2nd VIM	OUT	9 ± 1	60 ± 1	19 ± 3
2nd ESR	OUT	10 ± 1	65 ± 23	8 ± 1

*IN was calculated using the chemistry of the Cr and Co melt stock.

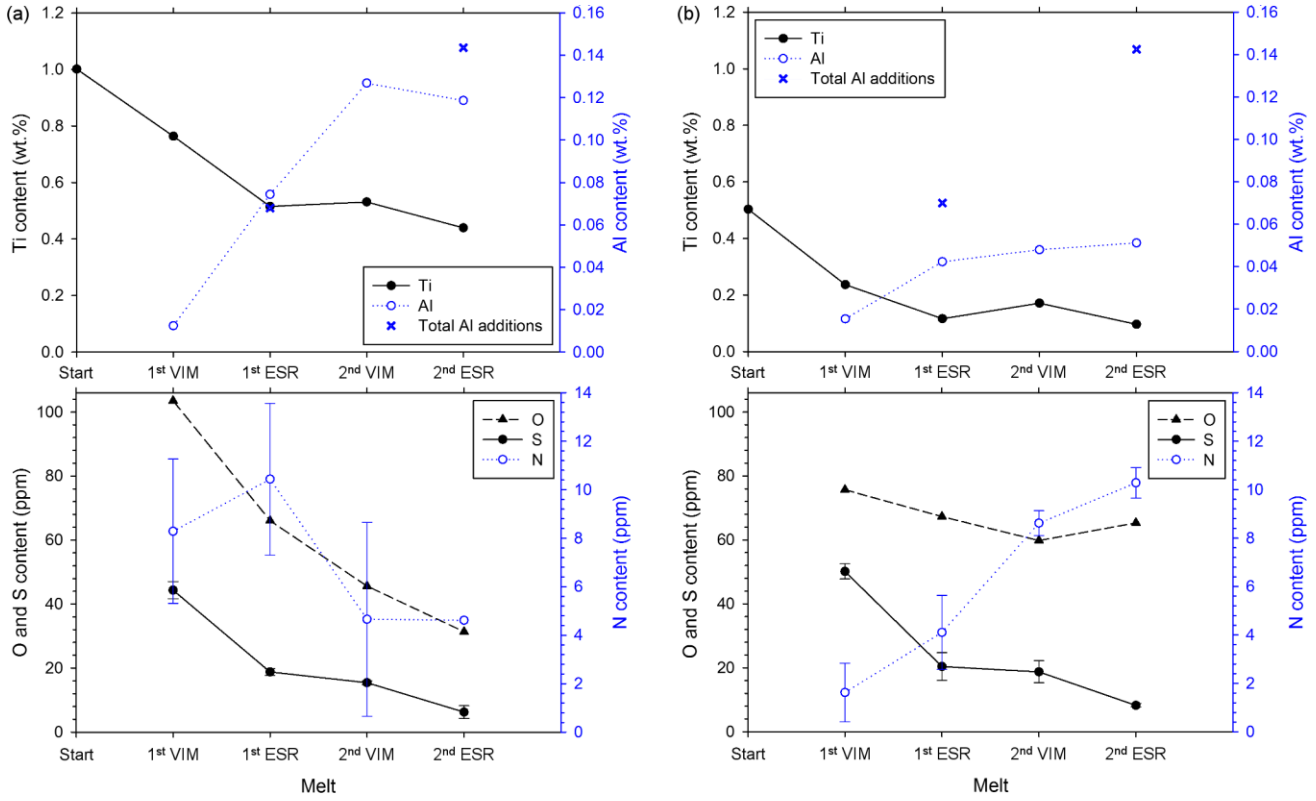

Figure 6. Chemistry results for (a) the binary Ni-25Cr and (b) the ternary Ni-30Co-30Cr master alloys showing the amount of Ti, Al, O, S, and N at each step of the melting process and the Al additions during ESR.

on the XRF samples after repolishing to 0.06 µm colloidal silica. A FEI Inspect F field emission scanning electron microscope (SEM) was employed with an accelerating voltage of 10 kV. Phase identification and composition measurements was performed using an Oxford Instrument energy dispersive spectroscope (EDS) attached to the SEM.

Results

The compositions of the master alloys measured after each step of the melting processes are listed in Tables II and III along with the various additions made during VIM and/or ESR. The evolution of the trace and tramp elements Ti, Al, N, O and S are plotted in Figure 6 for better observation of the resulting trends. The Cr and Co contents remained almost unchanged throughout the melting of the master alloys. The Ti content was found to decrease monotonically during the melting process (Table II and Figure 6) dropping from 1.00 to 0.44 wt.% and from 0.50 to 0.10 wt.% in the binary and ternary alloys, respectively. It should be noted that the Ti content at the end of second ESR of the ternary alloy was significantly lower than that of the binary alloy and the relative decrease from initial to final content was significantly greater with respect to the initial Ti content falling by 5x in the ternary vs. 2.3x in the binary. Interestingly, the evolution of the Al content throughout the melting process was found to be significantly different for the two master alloys as well. In both alloys, the Al content was generally found to increase after each melt, however, the overall increase was significantly greater during melting of the binary alloy than the ternary. In the binary alloy, the Al content was found to nearly follow the Al addition from the feeder during ESR, Figure 6. Finally, the carbon content was observed to remain constant, in view of the standard deviations, with final values of 377 and 290 ppm for the binary and ternary master alloys, respectively.

The nitrogen levels were kept low with minimum and maximum values of 2 and 10 ppm, respectively. Interestingly, the nitrogen content was found to increase after each melt of the ternary alloy, whereas, lower values were obtained after the second VIM and ESR of the binary alloy, Figure 6. The average oxygen level of all steps was similar for both alloys at approximately 62 ppm and 67 ppm for the binary and ternary alloys, respectively. The oxygen content was generally found to decrease as a result of each melt and the evolution is represented in Figure 6, however, the reader should use the oxygen plot with caution considering the standard deviations reported in Table III and removed from the plots for clarity. Finally, the sulfur content was found to decrease significantly following each ESR process with values from 44 to 6 ppm and 50 to 8 ppm in the binary and ternary alloys, respectively. Lower sulfur levels were found in the binary alloy compared to the ternary alloy, although the values are relatively close with regards to the standard deviations. It is evident from Figure 6 that a significant decrease in the amount of sulfur resulted from each ESR process.

SEM images of the binary sample cross sections are shown in Figure 7 and represent an overview of the inclusions present in the master alloys following each melt. Additionally, higher magnification images of the various inclusion types observed in

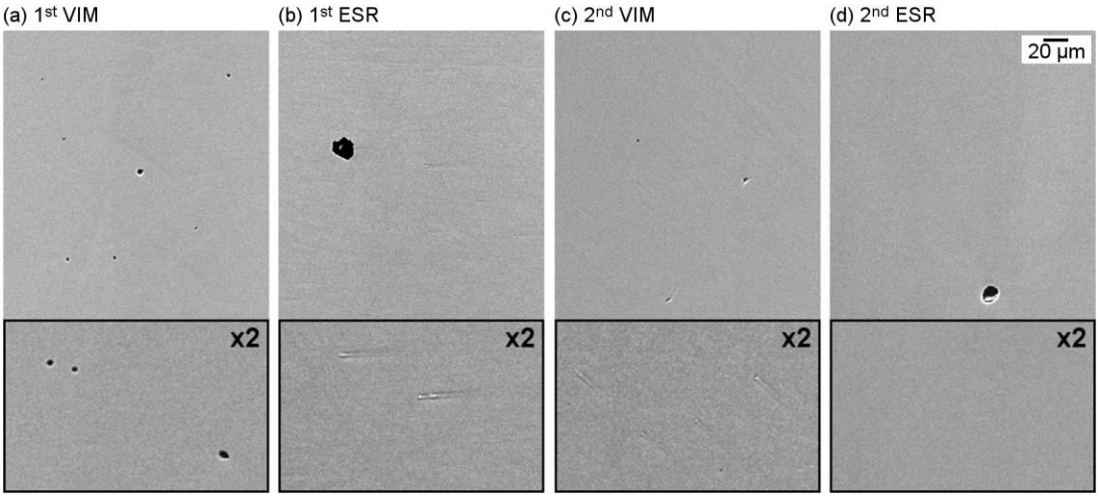

Figure 7. Overview SEM images of the binary master alloy after each melt.

Table IV. Inclusions found in the master alloys with average and standard deviations.

Inclusions	Partitioning	Diameter (µm)			
		1st VIM	1st ESR	2nd VIM	2nd ESR
TiO_2 / CrS	Cr / Ti	1.6 ± 0.5	3.7 ± 1.3	1.5 ± 0.4	1.7
Al oxide (serrated/void)	Cr	6.8 ± 2.7	12.8 ± 2.3	5.3 ± 1.8	8.8 ± 4.6
Al oxide (facetted)	Cr	-	4.0 ± 1.7	-	2.8 ± 1.4
Slag	Zr, Mg, Al, Cr, O	-	2.3 ± 1.0	2.8	1.8 ± 0.6
TiN	Cr /Slag, O core	-	-	-	1.4

both alloys are compiled in Figures 8 through 10. Finally, all inclusions types are listed in Table IV for each melt with their average diameters. It should be noted that a greater number of inclusions are expected to remain in the samples as compared to the rest of the ingot since the specimens were extracted from the bottom of the VIM ingots and top of the ESR ingots where freezing and floatation of inclusions can occur, respectively. From the overview image, Figure 7a, relatively small inclusions appear to be distributed all throughout the cross section of the binary alloy following the first VIM. Most of those inclusions were identified as Ti-containing CrS and Cr-containing TiO_2 and the average size was calculated at ~1.6 µm, Figure 8a and b. Those inclusions were observed in the bulk, coexisting, Figure 8c, or at the grain boundaries, Figure 8d. In addition, larger Cr-containing Al oxide inclusions were observed in fewer number and of average diameter of ~6.8 µm, Figure 8e and f. EDS measurements revealed a AlO_2 composition. Remelting of the VIM ingots resulted in considerably fewer CrS and TiO_2 inclusions and a cleaner microstructure, Figure 7b. However, large inclusions remained and additional facetted inclusions appeared throughout the microstructure. The average diameter of the CrS and TiO_2 inclusions was calculated at ~3.7 µm, more than twice the size of those observed in the VIM ingot. Often, the inclusions contained elements originating from the slag as impurities such as Mg and Zr. Few slag inclusions of relatively smaller size at ~2.3 µm were also observed, Table IV. The large inclusions observed in Figure 7b were similar to the Al oxides observed in the VIM ingot, although almost double in size with an average diameter of ~12.8 µm, Table IV. The morphology, with serrated edges and often pulled out leaving voids in the microstructure can be observed in Figure 9a and b. An additional type of inclusion was found to form during remelting. Smaller facetted Al oxides of average size ~4.0 µm, represented in Figure 9c-e and observed in Figure 7b on the magnified region. The Al oxide particles were found to contain Cr and sometimes presented a Cr-rich core. Subsequent melting of the ESR ingot during the second VIM step resulted in a complete dissolution of the larger facetted Al oxide phase, however, the smaller particles remained in the microstructure and are observed in Figure 7c on the magnified region. Aside from those, the serrated Al oxide inclusions were found to decrease in size following the second VIM step from 12.8 to 5.3 µm and fewer CrS and TiO_2 inclusions were observed with a size below that following the first VIM and remelting, Table IV. Final remelting of the master alloys resulted in significantly improved microstructures with overall fewer inclusions, Figure 7d. Very few CrS and TiO_2 inclusions were observed, the Al oxide serrated inclusions/voids presented an average size of 8.8 µm as compared to 12.8 µm following the first remelting, the size of the facetted Al oxides decreased from 2.8 to 1.8 µm, and the size of the slag inclusions decreased from 2.8 to 1.8 µm. Additionally, no fine facetted Al oxides remained in the microstructure, Figure 7d. One TiN was observed in the binary master alloy and its size was calculated at ~1.4 µm. Finally, one of the few differences observed between the inclusions found in the binary and ternary alloys is represented in Figure 10. The binary alloy contained a greater amount of the facetted Al oxides as compared to the ternary alloy. Those oxides presented a similar morphology as observed in Figure 9. Conversely, the ternary master alloy contained Al oxides of plate-like morphology, Figure 10b, that were not observed in the binary master alloy.

Discussion

The role of the alloying additions

Casting of simple binary or ternary master alloys from virgin melt stock can be challenging, not only because of the difference in the

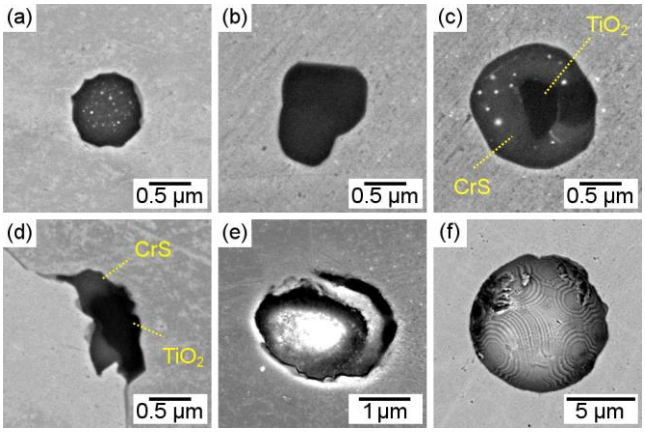

Figure 8. Inclusions following the 1st VIM with (a) CrS, (b) TiO_2, (c) CrS/TiO_2 core, (d) CrS/TiO_2 at a grain boundary, (e) Al oxide, and (f) void.

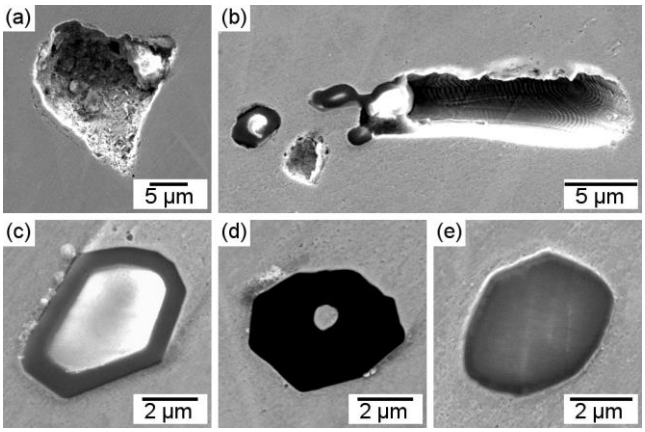

Figure 9. Al oxides observed following the 1st ESR of the master alloys. (a) void, (b) Al oxides and void, (c) Cr-containing Al oxide, (d) Cr core and (e) image at lower accelerating voltage (5kV).

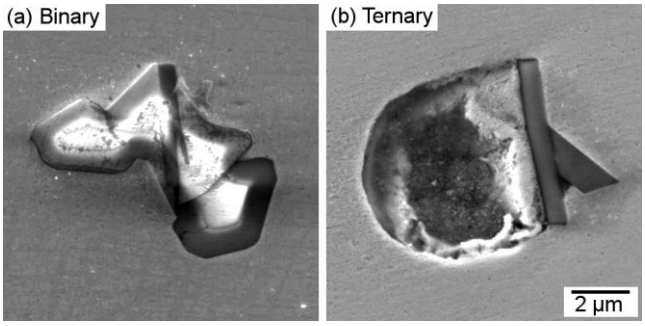

Figure 10. Al oxides in the (a) binary and (b) ternary master alloys following the 2nd ESR step.

melting temperatures, but also because of the differences in density (Cr tends to "float" during induction melting). During ESR, the narrow melt range can significantly impair the melting rate [21] and effectiveness of the refinement process by limiting the size and affecting the shape of the melt pool. Furthermore, fewer elements in the alloy composition could potentially restrict the interdendritic liquid flow [20]. The relatively small addition of carbon allowed the melt range to expand, Figure 1, and enabled a better control of melting around the liquidus temperature. Similarly, the Ti addition further expanded the liquid fraction lines, Figure 3a, and thus, both elements were beneficial to the melting characteristics of the master alloys.

Ti was added to the master alloy compositions to control the oxygen level during VIM. The trends represented in Figure 6 for both alloys suggest that Ti was consumed during the first VIM step and during each remelting process. Most of the oxygen originated from the raw Cr added to the first VIM. The presence of Ti allowed for the formation of TiO_2 resulting in overall low oxygen content in the alloys as the Ti-oxides are expected to remain on the surface of the solidified ingot, attach to the VIM skull and report to the slag. The smaller inclusions remaining in the ingot following VIM, Figures 7a and 8a-d, were likely dissolved in the molten slag during remelting, Figures 3b and 4. Therefore, considerably fewer Ti-oxides were observed in the microstructures of the ESR ingots, Figure 9 and Table IV. Although overall higher Ti concentrations were measured in the binary alloy, lower nitrogen levels were found towards the end of melting of the binary alloy while the nitrogen content was found to increase after each step of the melting process of the ternary alloy. This can be attributed to the likely dissolution of the inclusions in the molten slag or movement of the particles towards the outer diameter of the ingot due to the liquid metal flow [17]. Although, the simulations of Figure 4 predicted negligible influence of the Ti level on the inclusion motion, a higher probability of small TiN going into the ingot was predicted in the ternary alloy. This can be related to the thermo-physical properties of the alloys with lower densities, liquidus and solidus temperatures in the ternary alloy. Furthermore, the resulting differences in melt rates between the binary and ternary alloys can also be responsible for the number and size of inclusions reporting to the ingot as the melt rate relates to the time for floatation of inclusions within the melt pool [12].

The CFD predictions of Figures 3b and 4 provide an insight on the inclusion travel during remelting as a function of their size during ESR. A critical inclusion diameter of ~50 µm was found to result in a high probability of particles traveling into the ingot. Those preferentially travelled around the outer liquid flow loop and likely entered the ingot following the liquid fraction lines of Figure 3a, close to the crucible wall, Figure 11b. Below ~50 µm, the inclusions tended to travel around the slag region below the electrode and had a limited probability of ending in the ingot. Those inclusions likely dissolved in the slag or floated towards the slag/Ar interface, Figure 11c. Inclusions larger than the critical size tended to float and remain in the slag, Figure 11a. Thus, controlling the size of the inclusions created during VIM could potentially lead to a better control of the inclusion motion during ESR. Enabling the growth of particles to sizes greater than 70 µm during VIM could prevent them from traveling into the ingot. Going further, the inclusion/size simulations should be conducted for the densities of every inclusions expected to form during melting as the particle relative density affects the critical size.

The decrease in sulfur content observed in Figure 6 for both alloys was significant after each remelting step due to the desulfurization properties of ESR expressed in Equation 1. Going further, the benefit of the alloying additions on the sulfur levels can be assessed using the distribution coefficient of sulfur between the liquid metal and slag expressed by Nafziger et al. [16] as follows:

$$L = K\frac{P_{O^{2-}}}{[O]\gamma_{S^{2-}}} \quad (3)$$

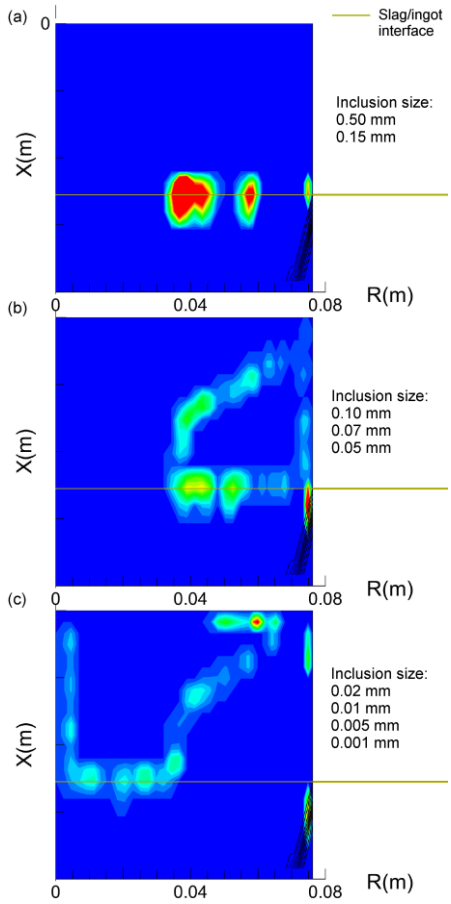

Figure 11. Predicted inclusion ending locations in the slag region and melt pool for various inclusion sizes.

In Equation 3, *K* is the equilibrium constant of the reaction between sulfur and oxygen, Equation 1, *P* is the partial pressure, γ is the activity coefficient, and [O] is the oxygen content in the metal. Therefore, low oxygen content in the metal [O] enhances the transfer of sulfur from the liquid metal to the slag [15]. This underlines the importance of a low oxygen content following VIM. This phenomenon was observed in the master alloys of this investigation. Comparatively lower sulfur levels were measured in the binary alloy that contained higher Ti concentrations at every step of the melting process compared to the ternary alloy, Figure 6 and Table II. The higher Ti concentration in the binary alloys potentially led to lower oxygen levels in the liquid metal drops traveling through the slag which likely enhanced desulfurization.

Al was used to further deoxidize the slag during remelting using additions from the feeder. Although overall low oxygen contents were measured in the alloys, the actual contribution of Al in decreasing the oxygen content is uncertain. The Al content was found to increase during the melting process for both alloys. Although no contamination from prior melting could occur due to the use of a new crucible, the crucible used during VIM was made of alumina. Consequently, a reaction between Cr and the crucible can explain the Al content measured following VIM using the following equation, where Al is transferred to the liquid metal:

$$2[Cr]_{metal} + (Al_2O_3)_{crucible} \rightarrow (Cr_2O_3)_{crucible} + [Al]_{metal} \quad (4)$$

Furthermore, considerable increases in the Al content were measured following remelting, particularly, during the first ESR step. This can be attributed to the Al added with the slag prior to steady state although the mechanisms by which the Al transfers to the liquid metal are not clear. Studies suggested that additions of reactive elements such as Ti can reduce the alumina in the slag [22,23] and the following reaction can be drawn:

$$3[Ti]_{metal} + 2(Al_2O_3)_{slag} \rightarrow 3(TiO_2)_{slag} + 4[Al]_{metal} \quad (5)$$

With Al added to the slag, Ti could react with the excess alumina which in turn could lead to Al pickup in the ingot. Our experimental results tend to agree with the suggested reaction as higher Al concentrations were measured overall in the binary alloy that contained a 1 wt.% initial Ti addition compared to the ternary with 0.5 wt.% Ti, Figure 6. Furthermore, a greater number of facetted Al oxides were observed in the binary alloy compared to smaller plate-like Al oxides in the ternary, Figure 10. Further work is ongoing to investigate the role of Al additions during ESR of Ni-Cr master alloys.

Usefulness of the master alloys

One of the criteria considered during the selection of the small additions of Ti and C was the residual amount in the composition of the master alloys. The final content should remain low enough and not exceed the levels specified in the alloys to be made using the master alloys. The carbon content remained relatively constant at ~300 ppm throughout the melting process, Table II. With the vast majority of C-containing commercial Ni-based superalloys having carbon contents exceeding 300 ppm [1], the master alloys of this investigation were readily usable in Ni-based superalloy formulation. Similarly, the remaining amount of Ti and Al were measured at 0.43 and 0.12 wt.% for the binary alloy and 0.09 and 0.04 wt.% for the ternary alloy and those concentrations are low when compared to Ti and Al containing commercial Ni-based superalloys.

Furthermore, the low amounts of tramp elements are particularly beneficial to the melting of Ni-based superalloys. Figure 12 represents the advances made at NETL on the control of nitrogen in Ni-Cr-Co and Ni-Cr based master alloys after the second ESR as a result of Ti additions. With no Ti added during VIM and raw Cr added during the second VIM step, the resulting nitrogen content in the final ESR ingot was measured at 110 ppm. No Ti additions and no raw Cr decreased the nitrogen content to 85 ppm. Finally, adding 0.5 and 1 wt.% Ti resulted in nitrogen contents of 10 and 5 ppm, respectively. To further illustrate the usefulness of those master alloys, Inconel 725 was designed for VIM using the binary master alloy of Figure 12 as source of Cr and Ni. The predicted nitrogen concentration was calculated based on the weight up to match the target composition and form a 7 kg ingot, assuming no nitrogen will originate from addition of the other constituting elements such as Al, Fe, Mn, Mo, Nb, Si, Ta, and Ti. Using the binary alloy from this investigation would lead to ~4 ppm nitrogen in the ingot while using the nitrogen content of the first ternary alloy in the composition of the master alloy would lead to ~92 ppm in the ingot. The resulting nitrogen content of several heats ranged from 6-17 ppm which shows the effectiveness of the clean master

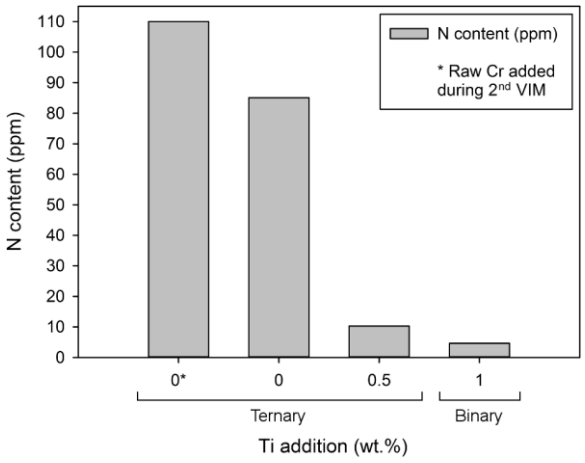

Figure 12. Nitrogen content measured following the 2nd ESR process of various master alloys fabricated at NETL as a function of the amount of Ti additions.

alloys. Thus, fewer inclusions would form during melting and solidification and the VIM process will produce a cleaner ingot.

Conclusions

Master alloys were fabricated using two iterations of VIM and ESR with targeted trace element additions to obtain low levels of deleterious elements. Nitrogen contents of 5 and 10 ppm, oxygen levels of 31 and 65 ppm, and sulfur levels of 6 and 8 ppm were measured in the final ingots of the binary and ternary alloys, respectively. Several conclusions were drawn from the results of this investigation:

1. Steps of VIM followed by ESR were beneficial to lowering the amount and size of inclusions in the ingots, the sulfur and oxygen content, and the added Ti concentration.
2. Minor carbon additions allowed the extension of the solidification range which improved and facilitated the remelting processes. The carbon content remained unchanged throughout the melting process.
3. Titanium additions were found to reduce the oxygen content during VIM through the formation of Ti-oxides and enhanced desulphurization during ESR. Most of the Ti-containing inclusions were removed during remelting.
4. Aluminum was used to deoxidize the slag during remelting, however, Al pickup was observed in the solidified ingots as well as the presence of relatively large Al-oxides. This was related to the excess alumina in the slag from the Al addition in the feeder favoring reactions with the Ti from the ESR electrode. Further work is ongoing to understand the role of Al additions in Ni-Cr master alloys.
5. CFD simulations give an insight on the inclusion motion during ESR as a function of their diameter. Controlling the size of the particles created during VIM can be beneficial to their removal during subsequent remelting. Particularly, large inclusions are predicted to float at the slag/metal interface and do not propagate into the ingot.

Acknowledgements

The authors would like to thank Mr. Edward Argetsinger and Mr. Joseph Mendenhall for assistance in melting. This research was supported in part by an appointment to the U.S. Department of Energy (DOE) Postgraduate Research Program at the National Energy Technology Laboratory administered by the Oak Ridge Institute for Science and Education.

Disclaimer

References

1. R.C. Reed, *The Superalloys: Fundamentals and Applications* (New York, NY: Cambridge University Press, 2006.)

2. Y. Zhang, T.T. Zuo, Z. Tang, M.C. Gao, K.A. Dahmen, P.K. Liaw, and Z.P. Liu, "Microstructures and properties of high-entropy alloys," *Progress in Materials Science*, 61 (2014), 1-93.

3. K. Harris and J.B. Wahl, "Developments in superalloy castability and new applications for advanced superalloys," *Materials Science and Technology*, 25 (2009), 147-153.

4. P.D. Jablonski and J.A. Hawk, "The Practical Application of Minor Element Control in Small Scale Melts," *Proceedings of the 2013 International Symposium on Liquid Metal Processing & Casting*, eds. M.J.M. Krane, A. Jardy, R.L. Williamson, and J.J. Beaman (Hoboken, NJ: John Wiley & Sons, Inc., 2013), 329-332.

5. M.A. Smith, W.E. Frazier, and B.A. Pregger, "Effect of sulfur on the cyclic oxidation behavior of a single crystalline, nickel-base superalloy," *Materials Science and Engineering A*, 203 (1995), 388-398.

6. S. Floreen and J.H. Westbrook, "Grain boundary segregation and the grain size dependence of strength of nickel-sulfur alloys," *Acta Metallurgica*, 17 (1969), 1175-1181.

7. K. Chen, L.R. Zhao, and J.S. Tse, "Sulfur embrittlement on γ/γ′ interface of Ni-base single crystal superalloys," *Acta Materialia*, 51 (2003), 1079-1086.

8. W.R. Sun, S.R. Guo, D.Z. Lu, Z.O. Hu, "Effect of sulfur on the solidification and segregation in Inconel 718 alloy," *Materials Letters*, 31 (1997), 195-200.

9. A. Mitchell, “Nitrogen in Superalloys,” *High Temperature Materials and Processes*, 24 (2005), 101-109.

10. J.D. Busch, J.J. DeBarbadillo, and M.J.M. Krane, “Flux Entrapment and Titanium Nitride Defects in Electroslag Remelting of INCOLOY Alloys 800 and 825,” *Metallurgical and Materials Transactions A*, 44 (2013), 5295-5303.

11. G. Hoyles, *Electroslag Processes: Principles and Practice* (New York, NY: Applied Science Publishers Co. Inc, 1983.)

12. A. Mitchell, “Solidification in remelting processes,” *Materials Science and Engineering A*, 413-414 (2005), 10-18.

13. J.O. Anderson, T. Helander, L. Hoglund, P.F. Shi, B. Sundman, “Thermo-Calc and DICTRA, Computational tools for materials science,” *Calphad*, 26 (2002), 273-312.

14. Thermo-Calc Software TCNI8 Nickel-based Alloys database version 8.

15. M. Eissa and A. El-Mohammadi, “Effect of physical properties of slag on sulfur removal mechanism during ESR process,” *Steel research*, 69 (1998), 413-417.

16. R.H. Nafziger, *The electroslag melting process* (United States Bureau of Mines, Bulletin 669, 1976.)

17. S.L. Cockcroft, T. Degawa, A. Mitchell, D.W. Tripp, A. Schmalz, “Inclusion precipitation in superalloys,” *Superalloys 1992*, eds. S.D. Antolovich, R.W. Stusrud, R.A. MacKay, D.L. Anton, T. Khan, R.D. Kissinger, D.L. Klarstrom (Warrendale, PA: The Minerals, Metals & Materials Society, 1992), 577-586.

18. K.M. Kelkar, S.V. Patankar, S.K. Srivatsa, R.S. Minisandram, D.G. Evans, J.J. deBarbadillo, R.H. Smith, R.C. Helmink, A. Mitchell, H.A. Sizek, “Computational Modeling of the Electroslag Remelting (ESR) Process Used for the Production of Ingots of High-Performance Alloys,” *Proceedings of the 2013 International Symposium on Liquid Metal Processing & Casting*, eds. M.J.M. Krane, A. Jardy, R.L. Williamson, and J.J. Beaman (Hoboken, NJ: John Wiley & Sons, Inc., 2013), 3-12.

19. N. Saunders, Z. Guo, X. Li, A.P. Miodownik, J.-Ph. Schille, “Using JMatPro to Model Materials Properties and Behavior,” *JOM*, 55 (2003) 60-65.

20. K. Fezi, J. Yanke, and M.J.M. Krane, “Macrosegregation During Electroslag Remelting of Alloy 625,” *Metallurgical and Materials Transactions A*, 46 (2015) 766-779.

21. P.D. Jablonski, M. Cretu, J. Nauman, “Considerations for the Operation of a Small Scale ESR Furnace,” *Proceedings of the 2017 International Symposium on Liquid Metal Processing & Casting*, (Cham, NY: Springer, 2017).

22. D.D. Wegman, “Investigation into critical parameters which determine the oxygen refining capability of the slag during electroslag remelting of alloy 718” (Ph.D. thesis, Lehigh University, 1983), Paper 180.

23. T.R. Bandyopadhyay, P.K. Rao, N. Prabhu, “Behavior of Alloying Elements during Electro-Slag Remelting of Ultrahigh Strength Steel,” *Electrometallurgy*, 4 (2012) 6-16.